The second second

Proceedings of the XIV International Symposium on Dynamic Problems of Mechanics (DINAME 2011), Fleury, A. T., Kurka, P. R. G. (Editors), ABCM, São Sebastião, SP, Brazil, March 13th - March 18th, 2011

Application of a Computer Vision Method and a Kalman Filter to Identify the Kinematics and the Dynamics of a Scaled-Model Riser

Martins, F.P.R. ¹, Trigo, F.C. ², Silva Jr., H.C. ³, Fleury, A.T. ⁴

Abstract: Aiming at overcoming the difficulties derived from the traditional camera calibration methods to record the underwater environment of a towing tank where experiments of scaled-model risers were carried on, a computer vision method, combining traditional image processing algorithms and a self-calibration technique was implemented. This method was used to identify the coordinates of control-points viewed on a scaled-model riser submitted to a periodic force applied to its fairlead attachment point. To study the observed motion, the riser was represented as a pseudo rigid body model (PRBM) and the hypotheses of compliant mechanisms theory were assumed in order to cope with its ellastic behaviour. The derived Lagrangian equations of motion were linearized and expressed as a state-space model in which the state variables include the generalized coordinates and the unknown generalized forces. The state-vector thus assembled is estimated through a Kalman Filter. The estimation procedure allows the determination of both the generalized forces and the tension along the cable, with statistically proven convergence.

Keywords: Dynamics, Kalman filter, compliant mechanisms, computer vision, motion analysis

NOMENCLATURE

 θ_i = PRBM's angular displacements

 $\dot{\theta}_i$ = PRBM's angular velocities

 $\hat{\theta}_i$ = PRBM's angular accelerations

K_i = PRBM's spring coefficients

 $K_{\theta} = PRBM$ 'standard spring coefficients

L = PRBM's bar lengths

γ = PRBM's largest bar length to actual bar length ratio

m = PRBM's bar mass

p = weigth per length ratio

p_s = underwater weight per length raio

E = material modulus of ellasticity

I = PRBM's bar section area inertia

T = kinetic energy

V = potencial energy

L = Lagrangian

 $F_{\theta i}$ = generalized force at node i

F = traction force

INTRODUCTION

The non-intrusive characteristics of the image-based instrumentation necessary to implement motion analysis is an important advantage of this approach compared to the classical measurement methods based on the use of accelerometers and load cells. Successive advances in the area of computer vision, concerning video segmentation, object tracking and camera calibration, have also contributed to the application of image-based methods to the analysis of kinematics phenomena that are difficult to measure, like the human motion (Moeslund *et al.*, 2006), or that occur in regions of difficult access, as the underwater environments (Shortis *et al.*, 2009).

Recently, this technique has been included in the palette of experimental methods of the Oceanic and Naval Engineering Center of IPT, in order to improve the quality of the measurements required by the hydrodynamics tests in a towing tank with scaled-models of ships and oceanic structures like platforms and risers. Although these measurements have been successfully accomplished with the aid of a comercial motion analysis tool, the camera calibration algorithms (Schalkoff, 1989) adopted by this software assume the use of calibration objects to previously measure the three-dimensional space according to a metrological procedure difficult to be done in an underwater environment

To cope with the various constraints imposed by the measurement environment, several camera self-calibration methods have been proposed in the literature (Hartley, 1997; Valdés and Ronda, 2005; Habed and Boufama, 2006; Menudet et al., 2007). Since these methods are based on invariant geometrical properties of the projective space (Veblen and Young, 1938; Ayres Jr., 1967), they do not depend on the use of calibration artifacts and, consequently, give rise to a calibrated space that is not limited by the volume of those objects. Such characteristics are specially helpful in the approach of underwater experiments with scaled-model risers (long flexible ducts used by the petroleum industry to pump oil and natural gas to the platforms).

¹ Escola Politécnica da Universidade de São Paulo, Av. Prof. Mello Moraes, 2231,S. Paulo, <u>flavius.martins@poli.usp.br</u>

² Escola Politécnica da Universidade de São Paulo, Av. Prof. Mello Moraes, 2231, S.Paulo, <u>flavio.trigo@poli.usp.br</u>

³ Instituto de Pesquisas Tecnológicas do Estado de S. Paulo, Av. Prof. Almeida Prado, 532, S.Paulo, helio.jr@ipt.br

⁴ Centro Universitário da FEI, Av. Humberto de Alencar Castelo Branco, 3972, S.B. do Campo, <u>ag.fleury@fei.edu.br</u>

Although the dynamics of cables has been longly approached in the early literature of theoretical mechanics (Beghin, 1952; Pérès, 1962), the recent technological advances observed in the petroleum industry concerning subsea fields extraction has fostered the research of this subject. Pesce (1997) performed a thorough investigation about the static and dynamic behaviours of risers under two-dimensional configurations. Using the theory of thin rods, it was shown that the effect of flexural rigidity is restricted to the regions close to the extremities of the riser; the dynamic model, on the other hand, was formulated as the solution of a perturbation problem around the equilibrium configuration. Both models – the static and the dynamic – were validated against experimental results. Using the finite element program ANSYS, Campos (1997) developed a computational non-linear model for a catenary riser, whose responses, concerning the dynamic bending moments near the touchdown point, are close to the ones derived from the application of previously proposed analytical models. Takafuji (2010), likewise, generated dynamical models through the finite element method, representing the catenary riser by beam elements. Firstly, a complete non-linear dynamical model was analysed using a time-domain technique. Then, the non-linearities of the original model were removed and a frequency-domain technique was applied, giving rise to results that compared well with the previous ones.

Considering that computer vision methods are not yet extensively adopted by the naval laboratories as a measurement tool, not so many works have been reported concerning application of those techniques to identify riser motions. Menezes (2008), aided by an image processing and computer graphics tool, constructed a computer vision procedure whose temporal estimates of the scaled model riser configuration were very close to the ones generated by a set of accelerometers fixed to the model. Using classical image segmentation algorithms, Amarante (2010) implemented a computer vision procedure to identify the temporal geometrical variations of a catenary riser near the touchdown point; in his work, the direct linear transformation was applied to map the Euclidean three-dimensional space to the projective two-dimensional spaces of the cameras.

In this article we explore the combination of a computer vision technique to measure the state variables that characterize the temporal configurations of a scaled-model riser and a Kalman filter that, using these measurements, estimates the state variables as well the generalized forces acting along the riser.

MATERIALS AND METHODS

A scaled-model riser, whose geometrical and physical characteristics are shown in Table 1, was submitted to a series of tests in a towing tank, where the flexible line assumed a typical catenary configuration, with its lower end anchored at the towing tank floor and its fairlead attachment point hinged to a harmonic oscilator assembled on a platform over the water line (Fig. 1). The riser motion is known from the time evolution of the locations of 200mm equally spaced small circular markers attached to the line, and is recorded by a high resolution video camera (JAI CV-A1) coupled to a varifocal lens (6mm-12mm). Connected to an asynchronous frame grabber (Coreco-Imaging PC2-Vision) and inserted on a water-proof canister installed inside the tank, the image acquisition system was set up to record up to 4MB monochromatic images of the region near the touchdown zone at the frequency of 100MB/s.

Table 1. Scaled-model riser: Geometrical properties, structural properties and distributed applied forces.

Length	8.190 m	Linear density	0.2190 kg/m
Diameter	0.254 m	Submerged linear density	0.1001 kg/m
Rigidity modulus	$1.337 \times 10^{-6} \text{ kg.m}^2$		

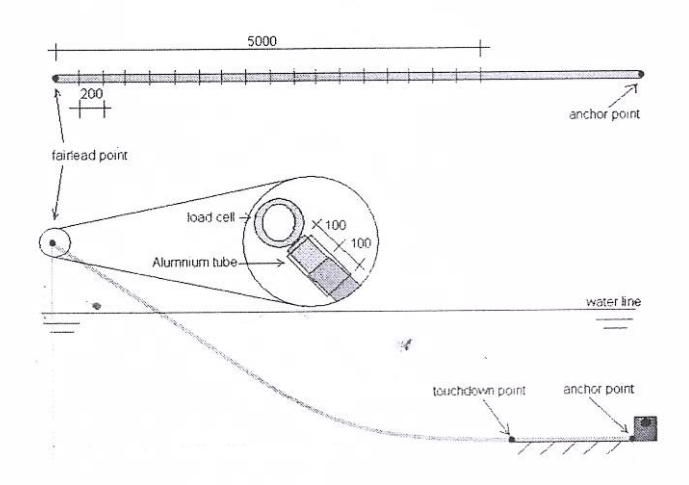


Figure 1 - Experimental setup.

Using the above referred image acquisition system, a series of images describing the planar motion of the scaled model riser were collected. As can be seen in Fig. 2a, the images generated by the experimental setup easily permit to estimate the inclination angle α between the image horizontal axis and the image towing bottom line. Furthermore, the measurement of distances between successive markers in the rotated image of Fig. 2b along its horizontal axis indicate that the horizontal scale does not change with position, i.e., that:

$$d_{1,2} = d_{2,3} = \cdots d_{n-1,n} = d \tag{1}$$

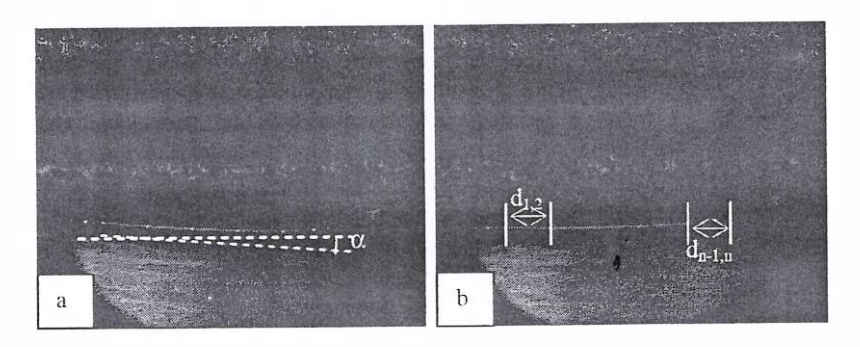


Figure 2. (a) Original image. (b) Image (a) rotated to align the towing bottom line with the horizontal axis.

The above results permit to assume that the projective transformation applied by the camera can be approximated by an affinity (see Fig. 3) with uniform horizontal and vertical scales estimated, respectively, by:

$$s_x = \frac{\ell}{d} \tag{2}$$

$$s_y^2 = \frac{(s_\theta s_x \sin \theta)^2}{s_x^2 - s_\theta^2 \cos^2 \theta}$$
(3)

where ℓ , the distance between markers, is a priori known (200mm), θ is the angle between the segment AB and the horizontal line and s_{θ} is the scale measured along the segment AB.

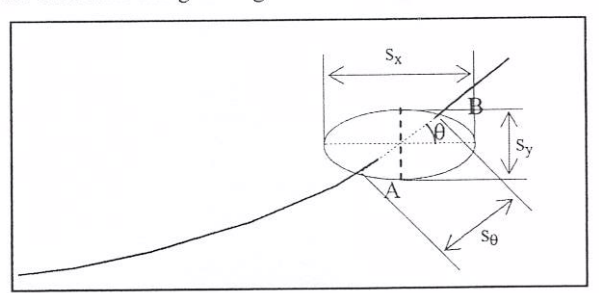


Figure 3. Measurement of the scale factors along a generic direction of the image plane.

After applying to the rotated images a segmentation process featured to isolate the image centroids (xim_i, yim_i) of the markers (see Fig. 4), their motion plane coordinates (x_i, y_i) were obtained by a simple scaling operation. So, observations of the scaled model riser kinematics could be properly described along the time.

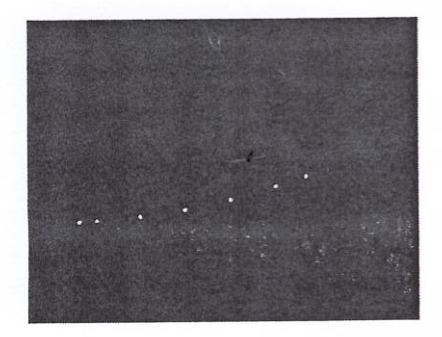


Figure 4. Identified markers of a segmented image.

Using the theory of compliant mechanisms (Howell, 2001), the scaled-model riser was represented as a pseudo rigid body model (PRBM) composed of segments of rigid bars linked by torsional springs (see Fig. 5) with constants that depend on the respective boundary conditions. As illustrated in Fig. 5, the number of degrees of freedom of the generated model is compatible with the observed kinematics data and the PRBM's equivalent compliant properties of the mechanism are calculated according to the expressions suggested by Weight (2001) concerning flexible beams submitted to some previously established load and boundary conditions.

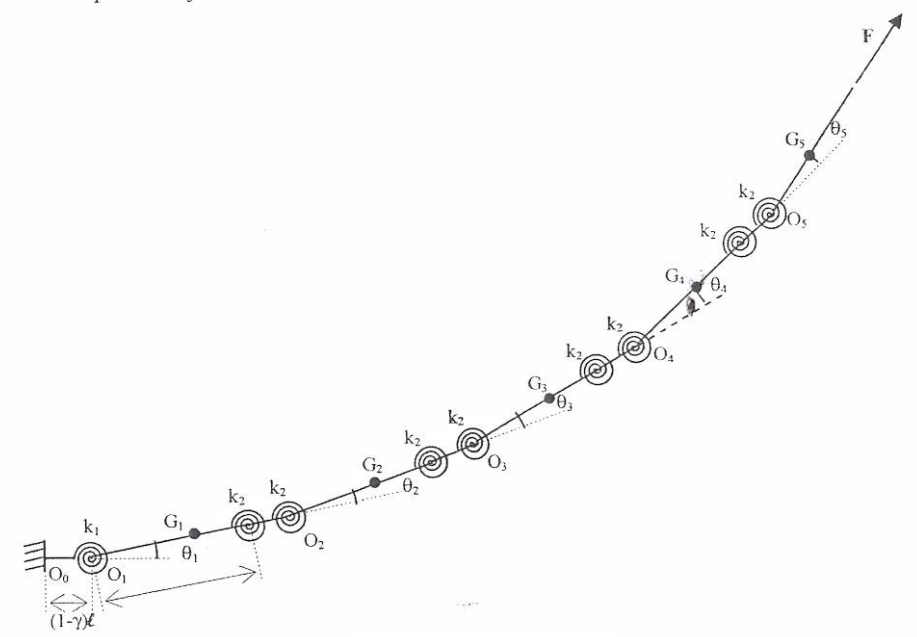


Figure 5. PRBM for the scaled model riser.

For the fixed-fixed beam boundary condition, the spring constant is:

$$K = \frac{2\gamma K_{\theta} EI}{\ell} \tag{4}$$

where, according to Howell (2001), γ =0.85 and K_{θ}=2.6.

Considering that all the springs or pairs of springs correspond to the same fixed-fixed beam boundary conditions, then:

$$k_1 = k_2 = K = \frac{2\gamma K_\theta EI}{\rho} \tag{5}$$

Moreover, the serial pairs of springs can be substituted by an equivalent spring with constant given by

$$k_2' = \frac{k_2}{2} = \frac{\gamma K_\theta EI}{\ell} \tag{6}$$

In order to write the Lagrangian equations for the compliant mechanism of Fig. 5, the expressions for the kinetic energy, the potential energy and the generalized forces were properly developed.

The kinetic energy is given by:

$$T = \frac{1}{2} \sum m_i v_{Gi}^2 + \frac{1}{2} \sum J_{Gi} \dot{\theta}_i^2 \tag{7}$$

where

$$\vec{v}_{Gi} = \vec{v}_{Oi} + \theta \vec{k} \wedge (G_i - O_i)$$
(8)

and J_{Gi} is the moment of inertia of the segment $O_{i-1}O_{i}$.

After substituting (8) in (7), the following expression for the kinetic energy results:

$$T = \frac{m\ell^{2}}{2} \left[\left(\frac{\gamma^{2}}{4} + 4 \right) \dot{\theta}_{1}^{2} + \left(\frac{\gamma^{2}}{4} + 3 \right) \dot{\theta}_{2}^{2} + \left(\frac{\gamma^{2}}{4} + 2 \right) \dot{\theta}_{3}^{2} + \left(\frac{\gamma^{2}}{4} + 1 \right) \dot{\theta}_{4}^{2} + \frac{\gamma^{2}}{4} \dot{\theta}_{5}^{2} \right] + \frac{m\ell^{2}}{2} \left[(6 + \gamma) \dot{\theta}_{1} \dot{\theta}_{2} \cos \theta_{2} + (4 + \gamma) \dot{\theta}_{1} \dot{\theta}_{3} \cos(\theta_{2} + \theta_{3}) + (2 + \gamma) \dot{\theta}_{1} \dot{\theta}_{4} \cos(\theta_{2} + \theta_{3} + \theta_{4}) \right] + \frac{m\ell^{2}}{2} \left[(2 + \gamma) \dot{\theta}_{2} \dot{\theta}_{3} \cos(\theta_{2} + \theta_{3} + \theta_{4} + \theta_{5}) \right] + \frac{m\ell^{2}}{2} \left[(4 + \gamma) \dot{\theta}_{2} \dot{\theta}_{3} \cos \theta_{3} + (2 + \gamma) \dot{\theta}_{2} \dot{\theta}_{4} \cos(\theta_{3} + \theta_{4}) + \gamma \dot{\theta}_{2} \dot{\theta}_{5} \cos(\theta_{3} + \theta_{4} + \theta_{5}) \right] + \frac{m\ell^{2}}{2} \left[(2 + \gamma) \dot{\theta}_{3} \dot{\theta}_{4} \cos \theta_{4} + \gamma \dot{\theta}_{3} \dot{\theta}_{5} \cos(\theta_{4} + \theta_{5}) + \gamma \dot{\theta}_{4} \dot{\theta}_{5} \cos \theta_{5} \right] + \frac{J}{2} \left[\dot{\theta}_{1}^{2} + \left(\dot{\theta}_{1} + \dot{\theta}_{2} \right)^{2} + \left(\dot{\theta}_{1} + \dot{\theta}_{2} + \dot{\theta}_{3} \right)^{2} + \left(\dot{\theta}_{1} + \dot{\theta}_{2} + \dot{\theta}_{3} + \dot{\theta}_{4} \right)^{2} + \left(\dot{\theta}_{1} + \dot{\theta}_{2} + \dot{\theta}_{3} + \dot{\theta}_{4} \right)^{2} + \left(\dot{\theta}_{1} + \dot{\theta}_{2} + \dot{\theta}_{3} + \dot{\theta}_{4} \right)^{2} \right]$$

The potential energy of the scaled-model riser encompasses the energy stored in the springs and the potential of the gravitational and hydrostatic forces. So, it is described by:

$$V = \frac{1}{2} \left(k_1 \theta_1^2 + k_2 \theta_2^2 + k_2 \theta_3^2 + k_2 \theta_4^2 + k_2 \theta_5^2 \right) +$$

$$p_3 \ell^2 \left[\left(4 + \frac{\gamma}{2} \right) \sin \theta_1 + \left(3 + \frac{\gamma}{2} \right) \sin \left(\theta_1 + \theta_2 \right) + \left(2 + \frac{\gamma}{2} \right) \sin \left(\theta_1 + \theta_2 + \theta_3 \right) \right] +$$

$$p_3 \ell^2 \left[\left(1 + \frac{\gamma}{2} \right) \sin \left(\theta_1 + \theta_2 + \theta_3 + \theta_4 \right) + \left(1 + \frac{\gamma}{2} \right) \sin \left(\theta_1 + \theta_2 + \theta_3 + \theta_4 + \theta_5 \right) \right]$$
(10)

where p_s is the underwater weight per length ratio.

The generalized force F_{θ} applied at the node O_5 , is:

$$F_{\theta i} = F_x \frac{\partial x_5}{\partial \theta i} + F_y \frac{\partial y_5}{\partial \theta i} \tag{11}$$

Adopting L=T-V and applying to Eq. (9) to (11) above the Lagrangian equations, given by:

$$\frac{d}{dt} \left(\frac{\partial L}{\partial \dot{\theta}_i} \right) + \left(\frac{\partial L}{\partial \theta_i} \right) = F_{\theta_i} \tag{12}$$

we obtain the following equations:

$$\frac{d}{dt}\left(\frac{\partial L}{\partial \dot{\theta}_{1}}\right) + \left(\frac{\partial L}{\partial \theta_{1}}\right) = F_{\theta 1} \implies$$

$$\left[m\ell^{2}\left(\frac{\gamma^{2}}{4} + 4\right) + 5J\right]\ddot{\theta}_{1} + \left[\frac{m\ell^{2}}{2}\left(6 + \gamma\right)\cos\theta_{2} + 4J\right]\ddot{\theta}_{2} + \left[\frac{m\ell^{2}}{2}\left(4 + \gamma\right)\cos\left(\theta_{2} + \theta_{3}\right) + 3J\right]\ddot{\theta}_{3} + \left[\frac{m\ell^{2}}{2}\left(2 + \gamma\right)\cos\left(\theta_{2} + \theta_{3} + \theta_{4}\right) + 2J\right]\ddot{\theta}_{4} + \left[\frac{m\ell^{2}}{2}\gamma\cos\left(\theta_{2} + \theta_{3} + \theta_{4} + \theta_{5}\right) + 3J\right]\ddot{\theta}_{5} - \frac{m\ell^{2}}{2}\left[\left(6 + \gamma\right)\sin\theta_{2}\dot{\theta}_{2}^{2} + \left(4 + \gamma\right)\sin\left(\theta_{2} + \theta_{3}\right)\dot{\theta}_{2}\dot{\theta}_{3} + \left(2 + \gamma\right)\sin\left(\theta_{2} + \theta_{3} + \theta_{4}\right)\dot{\theta}_{2}\dot{\theta}_{4} + \gamma\sin\left(\theta_{2} + \theta_{3} + \theta_{4} + \theta_{5}\right)\dot{\theta}_{2}\dot{\theta}_{5}\right] - \frac{m\ell^{2}}{2}\left[\left(4 + \gamma\right)\sin\left(\theta_{2} + \theta_{3}\right)\dot{\theta}_{3}^{2} + \left(2 + \gamma\right)\sin\left(\theta_{2} + \theta_{3} + \theta_{4}\right)\dot{\theta}_{3}\dot{\theta}_{4} + \gamma\sin\left(\theta_{2} + \theta_{3} + \theta_{4} + \theta_{5}\right)\dot{\theta}_{3}\dot{\theta}_{5}\right] - \frac{m\ell^{2}}{2}\left[\left(2 + \gamma\right)\sin\left(\theta_{2} + \theta_{3} + \theta_{4}\right)\dot{\theta}_{4}^{2} + \gamma\sin\left(\theta_{2} + \theta_{3} + \theta_{4} + \theta_{5}\right)\dot{\theta}_{4}\dot{\theta}_{4}^{2}\right] - \frac{m\ell^{2}}{2}\left[\gamma\sin\left(\theta_{2} + \theta_{3} + \theta_{4} + \theta_{5}\right)\dot{\theta}_{5}^{2}\right] + k_{1}\theta_{1} + \theta_{2}^{2}\dot{\theta}_{2}^{2} + \left(\frac{\gamma}{2} + 4\right)\cos\theta_{1} + \left(\frac{\gamma}{2} + 3\right)\cos(\theta_{1} + \theta_{2}) + \left(\frac{\gamma}{2} + 2\right)\cos(\theta_{1} + \theta_{2} + \theta_{3}) + \left(\frac{\gamma}{2} + 1\right)\cos(\theta_{1} + \theta_{2} + \theta_{3} + \theta_{4} + \theta_{5}) - F\ell[\sin\theta_{1} + \sin(\theta_{1} + \theta_{2} + \theta_{3} + \theta_{4} + \theta_{5})] - F\ell[\sin\theta_{1} + \sin(\theta_{1} + \theta_{2} + \theta_{3} + \theta_{4} + \theta_{5}) + F\ell[\cos\theta_{1} + \theta_{2} + \theta_{3} + \theta_{4}\right) + \cos(\theta_{1} + \theta_{2} + \theta_{3} + \theta_{4} + \theta_{5})]\sin(\theta_{1} + \theta_{2} + \theta_{3} + \theta_{4} + \theta_{5}) + F\ell[\cos\theta_{1} + \theta_{2} + \theta_{3} + \theta_{4}\right) + \cos(\theta_{1} + \theta_{2} + \theta_{3} + \theta_{4} + \theta_{5})]\sin(\theta_{1} + \theta_{2} + \theta_{3} + \theta_{4} + \theta_{5}) + F\ell[\cos\theta_{1} + \theta_{2} + \theta_{3} + \theta_{4}\right) + \cos(\theta_{1} + \theta_{2} + \theta_{3} + \theta_{4} + \theta_{5})]\sin(\theta_{1} + \theta_{2} + \theta_{3} + \theta_{4} + \theta_{5}) + F\ell[\cos\theta_{1} + \theta_{2} + \theta_{3} + \theta_{4}\right) + \cos(\theta_{1} + \theta_{2} + \theta_{3} + \theta_{4} + \theta_{5})]\sin(\theta_{1} + \theta_{2} + \theta_{3} + \theta_{4} + \theta_{5}) + F\ell[\cos\theta_{1} + \theta_{2} + \theta_{3} + \theta_{4}\right) + \cos(\theta_{1} + \theta_{2} + \theta_{3} + \theta_{4} + \theta_{5})]\sin(\theta_{1} + \theta_{2} + \theta_{3} + \theta_{4} + \theta_{5})$$

Application of Computer Vision Method to Identify Kinematics of a Scaled Riser Model

$$\frac{d}{dt} \left(\frac{\partial L}{\partial \theta_2} \right) - \frac{\partial L}{\partial \theta_2} = F_{\theta_2} \implies \frac{1}{2} \left[\frac{mt^2}{2} \left[2 + \gamma \right) \cos \theta_2 + 4J \right] \vec{\theta}_1 + \left[\frac{mt^2}{2} \left[\frac{\gamma^2}{2} + 6 \right] + 4J \right] \vec{\theta}_2 + \left[\frac{mt^2}{2} \left[(4 + \gamma) \cos \theta_1 + 3J \right] \vec{\theta}_3 + \left[\frac{mt^2}{2} \left[(4 + \gamma) \cos \theta_2 + 3J \right] \vec{\theta}_3 + \left[\frac{mt^2}{2} \left[(4 + \gamma) \cos \theta_2 + 3J \right] \vec{\theta}_3 + \left[\frac{mt^2}{2} \left[(4 + \gamma) \cos \theta_2 + 3J \right] \vec{\theta}_3 + \left[\frac{mt^2}{2} \left[(4 + \gamma) \cos \theta_2 + 3J \right] \vec{\theta}_3 + \left[\frac{mt^2}{2} \left[(4 + \gamma) \cos \theta_2 + 3J \right] \vec{\theta}_3 + \left[\frac{mt^2}{2} \left[(4 + \gamma) \cos \theta_2 + 3J \right] \vec{\theta}_3 + \left[\frac{mt^2}{2} \left[(4 + \gamma) \sin \theta_2 + \theta_3 \right] \vec{\theta}_2 + \left[\frac{mt^2}{2} \left[(4 + \gamma) \sin \theta_2 + \theta_3 \right] \vec{\theta}_3 + \left[\frac{mt^2}{2} \left[(4 + \gamma) \sin \theta_2 + \theta_3 \right] \vec{\theta}_3 + \left[\frac{mt^2}{2} \left[(4 + \gamma) \sin \theta_2 + \theta_3 \right] \vec{\theta}_3 + \left[\frac{mt^2}{2} \left[(4 + \gamma) \sin \theta_2 + \theta_3 \right] \vec{\theta}_3 + \left[\frac{mt^2}{2} \left[(4 + \gamma) \sin \theta_2 + \theta_3 \right] \vec{\theta}_3 + \left[\frac{mt^2}{2} \left[(4 + \gamma) \sin \theta_2 + \theta_3 \right] \vec{\theta}_3 + \left[\frac{mt^2}{2} \left[(4 + \gamma) \sin \theta_2 + \theta_3 \right] \vec{\theta}_3 + \left[\frac{mt^2}{2} \left[(4 + \gamma) \sin \theta_2 + \theta_3 \right] \vec{\theta}_3 + \left[\frac{mt^2}{2} \left[(4 + \gamma) \sin \theta_2 + \theta_3 \right] \vec{\theta}_3 + \left[\frac{mt^2}{2} \left[(4 + \gamma) \sin \theta_2 + \theta_3 \right] \vec{\theta}_3 + \left[\frac{mt^2}{2} \left[(4 + \gamma) \sin \theta_2 + \theta_3 \right] \vec{\theta}_3 + \left[\frac{mt^2}{2} \left[(4 + \gamma) \sin \theta_2 + \theta_3 \right] \vec{\theta}_3 + \left[\frac{mt^2}{2} \left[(4 + \gamma) \sin \theta_2 + \theta_3 \right] \vec{\theta}_3 + \left[\frac{mt^2}{2} \left[(4 + \gamma) \sin \theta_2 + \theta_3 \right] \vec{\theta}_3 + \left[\frac{mt^2}{2} \left[(4 + \gamma) \sin \theta_2 + \theta_3 \right] \vec{\theta}_3 + \left[\frac{mt^2}{2} \left[(4 + \gamma) \sin \theta_2 + \theta_3 \right] \vec{\theta}_3 + \left[\frac{mt^2}{2} \left[(4 + \gamma) \sin \theta_2 + \theta_3 \right] \vec{\theta}_3 + \left[\frac{mt^2}{2} \left[(4 + \gamma) \sin \theta_2 + \theta_3 \right] \vec{\theta}_3 + \left[\frac{mt^2}{2} \left[(4 + \gamma) \sin \theta_2 + \theta_3 \right] \vec{\theta}_3 + \left[\frac{mt^2}{2} \left[(4 + \gamma) \sin \theta_2 + \theta_3 \right] \vec{\theta}_3 + \left[\frac{mt^2}{2} \left[(4 + \gamma) \sin \theta_2 + \theta_3 \right] \vec{\theta}_3 + \left[\frac{mt^2}{2} \left[(4 + \gamma) \sin \theta_2 + \theta_3 \right] \vec{\theta}_3 + \left[\frac{mt^2}{2} \left[(4 + \gamma) \sin \theta_2 + \theta_3 \right] \vec{\theta}_3 + \left[\frac{mt^2}{2} \left[(4 + \gamma) \sin \theta_2 + \theta_3 \right] \vec{\theta}_3 + \left[\frac{mt^2}{2} \left[(4 + \gamma) \sin \theta_2 + \theta_3 \right] \vec{\theta}_3 + \left[\frac{mt^2}{2} \left[(4 + \gamma) \sin \theta_2 + \theta_3 \right] \vec{\theta}_3 + \left[\frac{mt^2}{2} \left[(4 + \gamma) \sin \theta_3 + \theta_3 \right] \vec{\theta}_3 + \left[\frac{mt^2}{2} \left[(4 + \gamma) \sin \theta_3 + \theta_3 \right] \vec{\theta}_3 + \left[\frac{mt^2}{2} \left[(4 + \gamma) \sin \theta_3 + \theta_3 \right] \vec{\theta}_3 + \left[\frac{mt^2}{2} \left[\frac{mt^2}{2} \left[\frac{mt^2}{2} \left[\frac{mt^2}{2} \left[\frac{mt^2}{2} \left[$$

$$\frac{d}{dt}\left(\frac{\partial L}{\partial \dot{\theta}_{5}}\right) - \frac{\partial L}{\partial \theta_{5}} = F_{\theta 5} \Rightarrow$$

$$\left[\frac{m\ell^{2}}{2}\gamma\cos(\theta_{2} + \theta_{3} + \theta_{4} + \theta_{5}) + J\right] \ddot{\theta}_{1} + \left[\frac{m\ell^{2}}{2}\gamma\cos(\theta_{3} + \theta_{4} + \theta_{5}) + J\right] \ddot{\theta}_{2} + \left[\frac{m\ell^{2}}{2}\gamma\cos(\theta_{4} + \theta_{5}) + J\right] \ddot{\theta}_{3} + \left[\frac{m\ell^{2}}{2}\gamma\cos(\theta_{4} + \theta_{5}) + J\right] \ddot{\theta}_{4} + \left[\frac{m\ell^{2}}{2}\frac{\gamma}{2} + J\right] \ddot{\theta}_{5} - \frac{m\ell^{2}}{2} \left[\gamma\sin(\theta_{2} + \theta_{3} + \theta_{4} + \theta_{5})(\dot{\theta}_{1}\dot{\theta}_{2} + \dot{\theta}_{1}\dot{\theta}_{3} + \dot{\theta}_{1}\dot{\theta}_{4} + \dot{\theta}_{1}\dot{\theta}_{5}) + \gamma\sin(\theta_{3} + \theta_{4} + \theta_{5})(\dot{\theta}_{2}\dot{\theta}_{3} + \dot{\theta}_{2}\dot{\theta}_{4} + \dot{\theta}_{2}\dot{\theta}_{5})\right] + \frac{m\ell^{2}}{2} \left[\gamma\sin(\theta_{4} + \theta_{5})(\dot{\theta}_{3}\dot{\theta}_{4} + \dot{\theta}_{3}\dot{\theta}_{5}) + \gamma\sin\theta_{5}\dot{\theta}_{4}\right] + \frac{m\ell^{2}}{2} \left[\gamma\sin(\theta_{2} + \theta_{3} + \theta_{4} + \theta_{5})\dot{\theta}_{1}\dot{\theta}_{5} + \gamma\sin(\theta_{3} + \theta_{4} + \theta_{5})\dot{\theta}_{2}\dot{\theta}_{5} + \gamma\sin(\theta_{4} + \theta_{5})\dot{\theta}_{3}\dot{\theta}_{5} + \gamma\sin\theta_{5}\dot{\theta}_{4}\dot{\theta}_{5}\right] + k_{2}\theta_{5} + p_{3}\ell^{2}\left[\frac{\gamma}{2}\cos(\theta_{1} + \theta_{2} + \theta_{3} + \theta_{4} + \theta_{5})\right] = 0$$
(17)

After linearizing the Eq. (13) to (17) above, we obtain:

$$\left[\frac{m\ell^{2}}{2}\left(\frac{\gamma^{2}}{2}+2\right)+5J\right]\ddot{\theta}_{1}+\left[\frac{m\ell^{2}}{2}\left(6+\gamma\right)+4J\right]\ddot{\theta}_{2}+\left[\frac{m\ell^{2}}{2}\left(4+\gamma\right)+3J\right]\ddot{\theta}_{3}+\left[\frac{m\ell^{2}}{2}\left(2+\gamma\right)+2J\right]\ddot{\theta}_{4}+\left[\frac{m\ell^{2}}{2}\gamma+J\right]\ddot{\theta}_{5}+\right]$$

$$\left[k_{1}\theta_{1}+p_{s}\ell^{2}\left(10+\frac{5}{2}\gamma\right)=F\ell(\theta_{2}+2\theta_{3}+3\theta_{4}+4\theta_{5})\right]$$

$$\left[\frac{m\ell^{2}}{2}\left(6+\gamma\right)+4J\right]\ddot{\theta}_{1}+\left[m\ell^{2}\left(\frac{\gamma^{2}}{4}+3\right)+4J\right]\ddot{\theta}_{2}+\left[\frac{m\ell^{2}}{2}\left(4+\gamma\right)+3J\right]\ddot{\theta}_{3}+\left[\frac{m\ell^{2}}{2}\left(2+\gamma\right)+2J\right]\ddot{\theta}_{4}+\left[\frac{m\ell^{2}}{2}\gamma+J\right]\ddot{\theta}_{5}+\right]$$

$$\left[\frac{m\ell^{2}}{2}\left(4+\gamma\right)+3J\right]\ddot{\theta}_{1}+\left[\frac{m\ell^{2}}{2}\left(4+\gamma\right)+3J\right]\ddot{\theta}_{2}+\left[m\ell^{2}\left(\frac{\gamma^{2}}{4}+2\right)+3J\right]\ddot{\theta}_{3}+\left[\frac{m\ell^{2}}{2}\left(2+\gamma\right)+2J\right]\ddot{\theta}_{4}+\left[\frac{m\ell^{2}}{2}\gamma+J\right]\ddot{\theta}_{5}+\right]$$

$$\left[\frac{m\ell^{2}}{2}\left(2+\gamma\right)+2J\right]\ddot{\theta}_{1}+\left[\frac{m\ell^{2}}{2}\left(2+\gamma\right)+2J\right]\ddot{\theta}_{2}+\left[\frac{m\ell^{2}}{2}\left(2+\gamma\right)+2J\right]\ddot{\theta}_{3}+\left[m\ell^{2}\left(\frac{\gamma^{2}}{4}+1\right)+2J\right]\ddot{\theta}_{4}+\left[\frac{m\ell^{2}}{2}\gamma+J\right]\ddot{\theta}_{5}+\right]$$

$$\left[\frac{m\ell^{2}}{2}\left(2+\gamma\right)+2J\right]\ddot{\theta}_{1}+\left[\frac{m\ell^{2}}{2}\left(2+\gamma\right)+2J\right]\ddot{\theta}_{2}+\left[\frac{m\ell^{2}}{2}\left(2+\gamma\right)+2J\right]\ddot{\theta}_{3}+\left[m\ell^{2}\left(\frac{\gamma^{2}}{4}+1\right)+2J\right]\ddot{\theta}_{4}+\left[\frac{m\ell^{2}}{2}\gamma+J\right]\ddot{\theta}_{5}+\right]$$

$$\left[\frac{m\ell^{2}}{2}\left(2+\gamma\right)+2J\right]\ddot{\theta}_{1}+\left[\frac{m\ell^{2}}{2}\left(2+\gamma\right)+2J\right]\ddot{\theta}_{2}+\left[\frac{m\ell^{2}}{2}\left(2+\gamma\right)+2J\right]\ddot{\theta}_{3}+\left[\frac{m\ell^{2}}{2}\gamma+J\right]\ddot{\theta}_{5}+k_{2}\theta_{5}+p_{5}\ell^{2}\frac{\gamma}{2}=0$$

$$\left[\frac{m\ell^{2}}{2}\gamma+J\right]\ddot{\theta}_{1}+\left[\frac{m\ell^{2}}{2}\gamma+J\right]\ddot{\theta}_{2}+\left[\frac{m\ell^{2}}{2}\gamma+J\right]\ddot{\theta}_{3}+\left[\frac{m\ell^{2}}{2}\gamma+J\right]\ddot{\theta}_{5}+k_{2}\theta_{5}+p_{5}\ell^{2}\frac{\gamma}{2}=0$$
(22)

The set of linearized differential Eq. 18-22 in the generalized coordinates must now be solved for those coordinates and for the unknown cable tension F, a forcing term that occurs at the right side of Eq. (18) to (21) and contribute to the bending moment at the end of each but the outermost right segment of the compliant mechanism model. In order to solve the stated problem, we formulate it as a state-space problem and use a Kalman filter to estimate the state, a vector containing the generalized coordinates and its derivatives plus the unknown forcing terms. The approach we used to obtain the state-space model is described next.

Equations (18) to (22) are a space discretized and time continuous representation of the compliant mechanism approach to the suspended cable problem; accordingly, they can be written as

$$[M]\ddot{\theta}(t) + [K]\theta(t) \stackrel{\mathcal{A}}{=} \Psi(t), \tag{23}$$

in which [M], $[K] \in \mathbb{R}^{5x5}$ are respectively the inertia and stiffness matrices, $\underline{\theta}(t) \in \mathbb{R}^{5x1}$ is a vector of generalized coordinates and $\underline{\Psi}(t) \in \mathbb{R}^{5x1}$ accounts for all terms that do not contain the generalized coordinates and their derivatives. As it is noticeable from Eq. (18) to (22), the continuous-time model thus assembled is coupled in the second

Application of Computer Vision Method to Identify Kinematics of a Scaled Riser Model

derivatives, i. e., matrix [M] is not diagonal; however, since it is real and simetric, it is possible to write a linear map $L: \underline{\theta} \to \eta$ such that

$$\underline{\theta}(t) = [L]\eta(t),\tag{24}$$

[L] being a square non-singular constant matrix or order 5. As a consequence of substitution of Eq. (24) into Eq. (23) and multiplying both sides by [L]^T, one obtains

$$[L]^{T}[M][L]\dot{\eta}(t) + [L]^{T}[K][L]\eta(t) = [L]^{T}\underline{\Psi}(t), \tag{25}$$

or, in shorter form,

$$[M_d]\ddot{\eta}(t) + [K_s]\eta(t) = \underline{\Omega}(t), \tag{26}$$

with $[M_d]$ a diagonal matrix and $[K_s]$ a simetric matrix, thus decoupling the system in the second derivatives of the generalized coordinates and allowing its description in a canonical state-space framework. In this work, we employed an appropriate built-in *Octave* function to obtain the transformation matrix $[L_i]$. The components of the state-vector are, then, $x_i(t)$, i = 1:10 with

$$\eta_1 = x_1$$
 $\eta_2 = x_3$
 \dots
 $\eta_5 = x_9$

$$\dot{\eta}_1 = x_2 = \dot{x}_1$$
 $\dot{\eta}_2 = x_4 = \dot{x}_3$
 \dots
 $\dot{\eta}_5 = x_{10} = \dot{x}_9$
(27)

For the ordinary case in which the forcing vector of the right-hand side of Eq. 26 is known, $\underline{x}(t) \in R^{10}$ would be the state-vector of the Kalman filter process model, represented in matrix form as

$$\underline{\dot{x}} = F_p \underline{x} + G_p \underline{\Omega}, \quad F_p \in R^{10x10}, G_p \in R^{10x5}$$
(28)

Nevertheless, since our interest is to estimate not only the generalized coordinates but also the forcing vector, we include those terms in the estimation problem by augmenting the ordinary state-vector. Firstly, we consider the forcing vector as the output of a linear filter driven by zero-mean Gaussian white noise:

$$\underline{\dot{x}}_f = F_f \underline{x}_f + G_f \underline{w}_f, \quad \underline{x}_f, \ \underline{w}_f \in R^5, \quad \underline{w}_f \sim N(0, Q)
\underline{y}_f = H_f \underline{x}_f$$
(29)

Equations (29), in which F_f , G_f and H_f are identitity matrices of order 5, exhibit respectively the state-space process and observation models for the unknown forcing vector $\underline{\Omega}(t) = \underline{x_f}(t)$. Next, those equations are used to augment the system and observation state-space models for the original generalized coordinates according to Eq. (30),

$$\left\{ \frac{\dot{x}}{\dot{x}_f} \right\} = \begin{bmatrix} F_p & G_p H_f \\ 0_{5x10} & F_f \end{bmatrix} \underbrace{\left\{ \underline{x}_f \right\}}_{f} + \begin{bmatrix} 0_{10x5} \\ G_f \end{bmatrix} \underline{w_f} \qquad \Rightarrow \underline{\dot{X}} = A\underline{X} + B\underline{w}_f, \ A \in \mathbb{R}^{15x15}, \ B \in \mathbb{R}^{15x5}, \quad (30)$$

that provide the process state-space model in which both the generalized coordinates and the forcing terms constitute the state variables to be estimated. In view of Eq. (28) and (29), it should be emphasized that process uncertainties, expressed by the random vector \underline{w}_f are implicitly assumed to be restricted to the unknown forcing terms. This is a feasible assumption, since the simplification introduced by modeling the actual experimental riser as two-bar compliant mechanism according to Howell (2008) is capable of reproducing large displacements of an actual continuous beam, whose elastic curve results from the solution of an elliptical differential equation.

The observation equation for the augmented model will be assembled taking into account that the only measurements available are angular displacements of the bars, obtained from images grabbed by a video camera. Those images, through a segmentation procedure, provide Cartesian coordinates of a set of markers that are used to generate the correspondent angles. Inherent errors in the image segmentation procedure are modeled as zero-mean Gaussian noise with covariance matrix R, allowing for the observation equation to be written as

$$\underline{Y} = \begin{bmatrix} H_P & 0_{5x5} \end{bmatrix} \underline{X} + \underline{v} \quad \Rightarrow \underline{Y} = H \underline{X} + \underline{v}, \quad H_P \in \mathbb{R}^{5x10}, \ \underline{v} \in \mathbb{R}^5, \ \underline{v} \sim N(0, \mathbb{R}), \tag{31}$$

The state-space representation of the riser dynamical model according to Eq. (30) and (31) is hybrid (continuous-discrete), since the state evolves continuously, whereas measurements are available at specific sample times. For computational purposes, in this work the continuous process model was discretized (with the aid of a built-in function in

Octave) using the same time step-size as that of the measurements, i.e, each k^{th} iteration of the filter corresponds to a new measurement available. The obtained discrete-time process model is, then,

$$\underline{X}(t_k) = \Phi(t_k, t_{k-1})\underline{X}(t_{k-1}) + B_d(t_k)w_f(t_k), \tag{32}$$

in which $\underline{X}(t_k)$ is the state vector k^{th} time step $k\Delta t$, $\Phi(t_k, t_{k-1})$ is the discrete-time transition matrix, and $B_d(t_k)w_f(t_k)$ is the discrete-time forcing vector. Accordingly, the discrete-time observation equation is

$$\underline{Y}(t_k) = H\underline{X}(t_k) + \underline{v}(t_k). \tag{33}$$

Regarding the estimation procedure, it suffices to mention that recursive estimation theory based on Kalman filtering is extensively discussed in the literature, see for instance Jazwinski (1970); thus, for the moment, we only state the hypotheses used and provide a brief explanation of the algorithm through its equations. As already mentioned, white noise sequences \underline{w}_f and \underline{v} are assumed zero-mean Gaussian with associated covariance matrices; in addition, those sequences are considered mutually independent and, as a consequence of being Gaussian, they are also uncorrelated. Covariance matrices Q and R are admitted constant and diagonal, whose plements are the variances of each state-variable.

For the model given by Eq. (32) and (33), there is a forecast stage that seeks to produce the best estimates (in a stochastic least-squares sense) by propagating the previous estimated state based on the process model and its known (or admitted) statistics before new information is available. This way, Eq. (34)

$$\underline{X}^{f}(t_{k}) = \Phi \underline{X}^{u}(t_{k-1}) \tag{34}$$

provides the state estimation forecast and eq. (35)

$$P^{f}(t_{k}) = P^{u}(t_{k-1}) + Q(t_{k-1})$$
(35)

gives the estimation error covariance matrix forecast. When new data is available, an update stage provides proper correction to the forecasted estimates of the state and error covariance according to Eq. (36) and (37),

$$\underline{X}^{u}(t_{k}) = \underline{X}^{f}(t_{k}) + K(t_{k}) \{\underline{y}(t_{k}) - H\underline{X}^{f}(t_{k})\}$$
(36)

$$P^{\mu}(t_k) = \left(I - K(t_k)H\right)P^{f}(t_k) . \tag{37}$$

It must be pointed out that in Eq. (36), $\underline{y}(t_k)$ is employed to represent the measurement vector, distinct from $\underline{Y}(t_k)$, measurement model.

The correction is provided by the Kalman gain matrix, computed according to Eq. (38)

$$K(t_k) = P^f(t_k)H\{HP^f(t_k)H^T + R(t_k)\}^{-1},$$
 (38)

thus completing the prediction-correction steps necessary for the next iteration of the filter.

RESULTS AND DISCUSSION

The previously described experimental setup grabbed images at a rate of 28 frames/s, thus providing observations of the position of each one of the five markers attached to the suspended cable at every 0.036 seconds. Computed Cartesian coordinates of the markers were used to get the effective angular observations for the Kalman filter estimation procedure. The covariance matrices were $Q=0.9 I_{I5}$ (process model noise covariance matrix, assumed constant), $R=0.01 I_{I5}$ (measurement model noise covariance matrix, assumed constant) and $P_0=0.5 I_{I5}$ (state-estimation error covariance matrix); the initial state-vector was

 $\left[-0.0183; \, 0.0276; \, 0.0085; \, 0.0262; \, 0.0633; \, 0.253; \, -0.5087; \, 0.011; \, 0.245; \, -0.189; \, 0.0376; \, 0.025; \, 0.0153; \, 0.0063; \, 0.0 \right]^T,$

obtained as the mean value of measurements from the three first frames grabbed. The last 5 state-variables correspond to bending moments computed using a static estimate of the traction force on the cable, F=0.5 N.

Estimates for the state-variables angular displacement and rotation are shown in Figs. 6 and 7. Those ten variables are the ones of the "original" dynamical system, i.e., without the augmentation that included forcing terms as state variables to be estimated. From Fig. 6, one realizes that the results are coherent since angular displacements have higher amplitudes for those nodes close to the left-side of the cable; in addition, angular velocities behave accordingly, see Fig. 7.

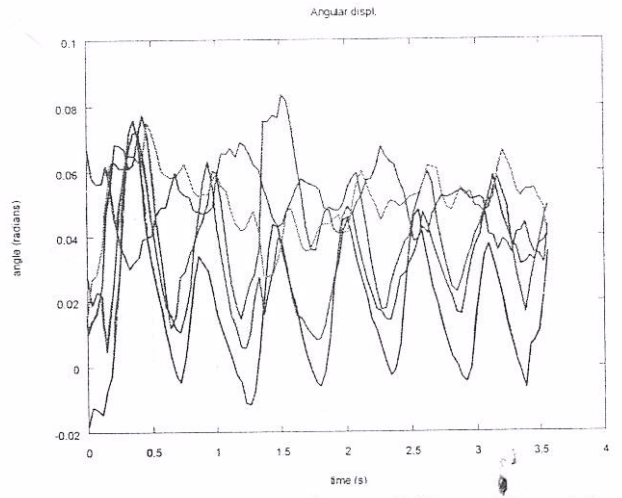


Figure 6: Angular displacements of the model bars at the rotational springs.

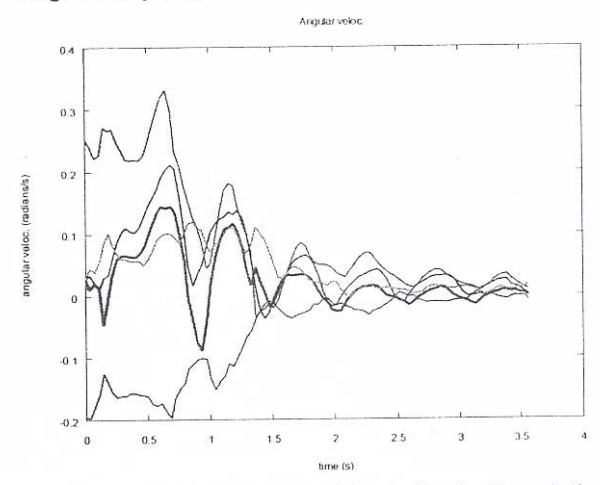


Figure 7: Angular velocity of the model bars attached to rotational springs.

Results of generalized forces depicted on Fig. 8 also corroborate the previous assertions, for moments (in this case, generalized forces are bending moments at the edge of each pair of bars setting) at the left-side of the cable present higher amplitudes, that decrease in the direction of the right-side. Particularly interesting is that, for the generalized force corresponding to state-variable number 15, the bending moment at the free-end of the cable, as shown by the purple curve, has mean value around zero from 2.5 seconds onward (the actual mean value in this range is -0.0058 N.m), complying with what was theoretically expected.

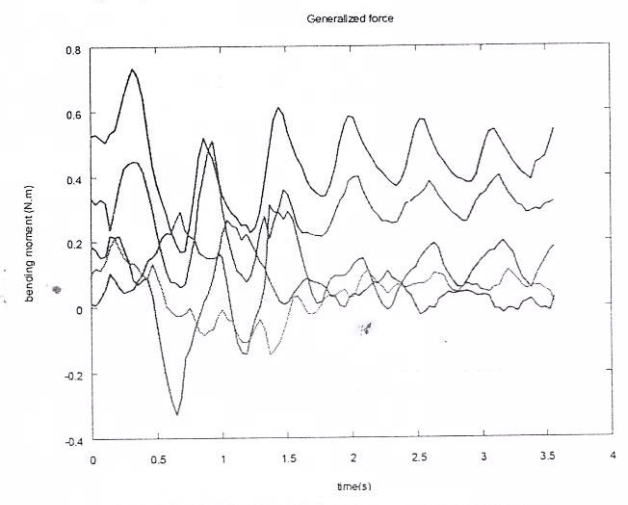


Figure 8: Estimates of generalized forces.

When the generalized forces, the 11th to 15th state-variables of the augmented state-space model are used to compute tension values on the string, its mean value is 10.9 N for the values calculated from curves representing state-variables 11 to 14, as seen of Fig. 9; regarding the 15th state-variable, its mean value is zero, for the same reasons stated above. It is as well worthwhile to mention that curves representing state-variables 11 to 14 present peaks whose amplitudes is decreasing, therefore suggesting that, if more observations were available, the estimates would converge to the above-mentioned mean value.

In order to support the assertions of the last paragraph, two evidences of the convergence of the estimation procedure are provided by the behaviour of the error covariance matrix and the normalized residual. The Euclidean norm of the estimation error covariance matrix $P^u(t_k)$ during the estimation process is depicted in Fig. 10, from which it is possible to realize that, after great amplitudes at the beginning of the process, once more observations are availabe, the error decreases and reaches a steady-state value, which indicates that the procedure has converged. This condition is, however, not enough to guarantee the actual convergence. As stated by Jazwinski (1970), actual convergence of the estimation process must be asserted by the inspection of the observation the difference between the effective measurement and its value as calculated by the filter using the last available state estimate. An estimation process is considered convergent once the normalized observation residuals is zero-mean Gaussian with standard deviation between $-3\sigma_v$ and $3\sigma_v$, given by Eq. (39)

$$r_{v} = \frac{1}{\ell \sigma_{v}} \sum_{j=1}^{\ell} (\underline{Y}_{j}(t_{k}) - \underline{X}_{j}^{f}(t_{k})) , \qquad (39)$$

where ℓ represents measurement vector dimension, in our case, $\ell=5$. In Fig. 11, it is shown that those requirements are fulfilled, because $E[r_v] = 0.012$ and $E[r_v^2] = 0.17$; therefore, one concludes that the procedure actually converges.

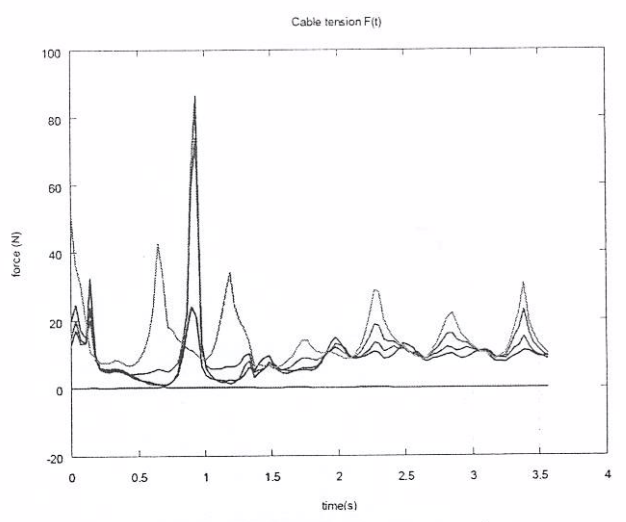


Figure 9: Estimates of cable tension.

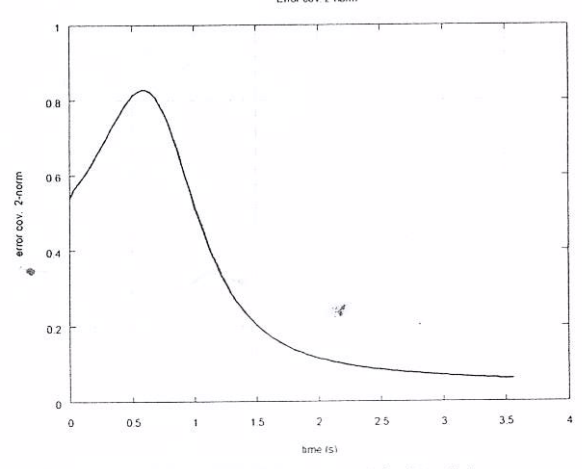


Figure 10: Error covariance matrix Euclidean norm.

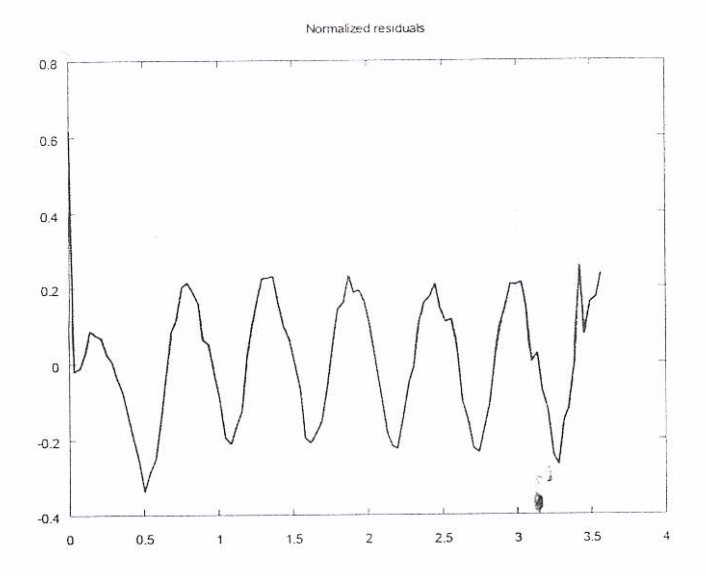


Figure 11: Normalized observation residuals.

CONCLUSIONS

This work investigated the use of a new approach to analyse the dynamics of an underwater suspended cable though image-based instrumentation associated to parameter estimation techniques. A scaled-model riser has undertaken several tests in a controlled environment. Simple self calibration procedures applied to images grabbed by a video camera provided observations used in a state-space model of the system dynamics obtained from the application of compliant mechanisms theory to spatially discretize the riser specimen. The system dynamical model was simulated through a linear Kalman filter in which the state-variables of the augmented state-space vector included the unknown generalized forces at the end of each discretized segment of the cable. Results from the simulations suggest that it is possible to use the described approach to estimate both the bending moments along the cable and the tension force at its free extremety. This assertion is corroborated by statistical evidence of the convergence of the filtering process, namely, decreasing error covariance matrix Euclidean norm and consistency of the normalized observation resuduals.

ACKNOWLEDGMENTS

This work was supported by CNPq as part of the project 471880/2006-0 – "Identificação da Cinemática de Embarcações e Estruturas Oceânicas Utilizando Visão Computacional". Fourth author also gratefully acknowledges CNPq for financial support.

REFERENCES

Amarante, R.M., 2010, "Estudo da estatática e dinâmica de linhas, sob configuração de catenária, através da identificação geométrica, processamento e análise de imagens digitais". Dissertação de mestrado, Escola Politécnica, Universidade de São Paulo.

Ayres Jr, F., 1967, "Theory and Problems of Projective Geometry". Schaum Publishing Co.

Beghin, H., 1952, "Mécanique Théorique et Appliquée", Tome 1. Gauthier-Villars, 551p.

Campos, L.A., 1997, "Análise de esforços dinâmicos na região do 'touchdown point' de um riser rígido em catenária". Dissertação de mestrado, Escola Politécnica, Universidade de São Paulo.

Gonzalez, R., Woods, R.E., 2002, "Digital Image Processing". Prentice-Hall, 2nd edition, 793p.

Habed, A., Boufama, B., 2006, "Camera Self-Calibration from Bivariate Polynomial Equations and Coplanarity Constraints". Image and Vision Computing, 24, pp.498-514.

Hartley, R.I., 1997, "Self-Calibration of Stationary Cameras". International Journal of Computer Vision, 22(1), pp. 5-23. Jazwinksi, A.H., 1970, "Stochastic Processes and Filtering Theory", Academic Press, New York, USA, 376 p.

Menezes Jr., L.F., 2008, "Processamento de imagens na análise dinâmica de risers de produção de petróleo com modelo de escala reduzida em ambiente de laboratório". Tese de doutorado, Faculdade de Engenharia Mecânica, Unicamp.

Menudet, J.F., Becker, J.M., Fournel, T., Menessier, C., 2007, "Plane-Based Camera Self-Calibration by Metric Rectification of Images". Image and Vision Computing, pp.1-22.

- Moeslund, T.B., Hilton, A., Krüger, V., 2006, "A Survey of Advances on Vision-Based Human Motion Capture and Analysis", Computer Vision and Image Understanding, 104, pp. 90-96.
- Pérès, J., 1962, "Mécanique Générale". Masson & Cie, 407p.
- Pesce, C.P., 1997, "Mecânica de cabos e tubos submersos lançados em 'catenária': uma abordagem analítica e experimental". Tese de livre-docência, Escola Politécnica, Universidade de São Paulo.
- Shortis, M., Harvey, E., Abdo, D., 2009, "A Review of Underwater Stereo Image Measurement for Marine Biology and Ecology Applications", Oceanographic and Marine Biology: An Annual Review, 47, pp. 257-292.
- Schalkoff, R.J., 1989, "Digital Image Processing and Computer Vision". John Wiley and Sons.
- Takafuji, F.C.M., 2010, "Dinâmica tridimensional de risers". Tese de doutorado, Escola Politécnica, Universidade de São Paulo.
- Valdés, A., Ronda, J.I., 2005, "Camera Autocalibration and the Calibration Pencil". Journal of Mathematical Imaging and Vision, Vol.23, pp. 167-174.
- Veblen, O., Young, J.W., 1938, "Projective Geometry", vol. 1, 2. The Athenaeum Press.
- Weight, B.L., 2001, "Development and design of constant-force mechanisms". Thesis. Brigham Young University, Department of Mechanical Engineering.

RESPONSIBILITY NOTICE

The authors are the only responsible for the printed material included in this paper.